Numerical investigation on the generation mechanism of aero-heating of rudder shaft from three-dimensional flow separation and vortices

Mingyue Lin (林明月) ; Fan Yang (杨帆) ; Chun Wang (王春) ✉

🔄 Check for updates

CrossMark

🌐 View Online

📄 Export Citation

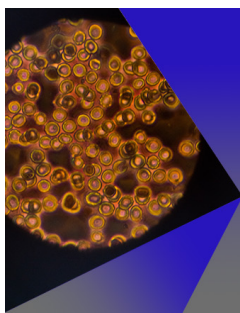**Articles You May Be Interested In**

Flow field analysis of rudder in CFD

AIP Conference Proceedings (February 2021)

Dynamic modeling and characteristic analysis of piezoelectric rudder actuator

Rev Sci Instrum (January 2019)

Hull-propeller-rudder interaction of the JBC ship model

AIP Conference Proceedings (November 2020)

Numerical investigation on the generation mechanism of aero-heating of rudder shaft from three-dimensional flow separation and vortices

View Online   Export Citation   CrossMark

Mingyue Lin (林明月),[1,2] (ID) Fan Yang (杨帆),[1,2] (ID) and Chun Wang (王春)[1,2,a] (ID)

AFFILIATIONS

[1] State Key Laboratory of High-Temperature Gas Dynamics, Chinese Academy of Sciences, 100190 Beijing, People's Republic of China
[2] School of Engineering Science, University of Chinese Academy of Sciences, 100049 Beijing, People's Republic of China

[a] Author to whom correspondence should be addressed: wangchun@imech.ac.cn

ABSTRACT

The hypersonic flow past a controlled rudder mounted at a gap to the aircraft fuselage is numerically investigated by solving three-dimensional (3D) Reynolds-averaged Navier–Stokes equations. This paper aims to explain the mechanism of production of extreme thermal environment faced by a rudder shaft from the view of physics of flow in the mounting gap. Simulations are conducted at Mach number of 10, and the gap ratio h/δ varies from 0 to 1.42, where h denotes the gap height and δ represents the thickness of the incoming turbulent boundary layer. Topological theory is utilized to identify the separation types. The formation of vortices is traced by extracting volume streamlines in the 3D space. The results indicate that the types of 3D separation appear in the gap shifts from the coexistence of horseshoe-type and tornado-type separations to only horseshoe-type separation that persists with the increase of h/δ. It is found that high heat flux is generated by the high-momentum fluid transported toward the surface by the horseshoe vortices. The tornado-type vortex prevents the incoming flow from arriving at the rudder shaft, which avoids the generation of high heat flux at the center of the rudder shaft. The rate of local heat transfer increases with h/δ as a result of the shrink and disappearance of the tornado-type vortices, which means that the region of low-speed backflow in front of the rudder is reduced and vanished. This study contributes to a clearer understanding of the flow physics in the complex disturbance area.

I. INTRODUCTION

Aero-heating is one of the key phenomena restricting the aero-performance of high-speed aircrafts. The design of a thermal protection system (TPS) in the future puts forward higher requirements for accurate predictions of aero-heating. The assessment of prediction of heat flux in the interference region of rudder/body poses a big challenge for the design of a TPS. Extensive studies have been conducted on the prediction of thermal environment in this region. In most of the studies, the rudder was reduced as simple figures, such as sharp un-swept[1–3]/swept fin[4] and blunt fin,[5–9] fixed to the fuselage without any surface imperfections.

From a practical perspective, the effect of geometric imperfections on the flow structures and aerothermodynamics of the interference region has received relatively little attention. Surface imperfections, such as coves or gaps, can introduce more complex flow structures and more severe aerothermal environments than the simple figures, according to the limited available research.[10] The cove is defined as the area between the wing's trailing-edge and elevon, which is required to allow for elevon deflection. Deveikis and Bartlett[11] experimentally investigated the heating rate of the cove region for a shuttle-type re-entry vehicle. Results indicated that the heating rate increased by an order of magnitude over the values of corresponding attached-flow when the flow separated at the cove entrance. Hunt[12] carried out a series of tunnel tests to study the flow patterns in the wing–elevon junction and determined the pressure and heat load within the chordwise gaps. The results showed that gap heating is proportional to wing heating and varies inversely with the

gap width. Wieting et al.[13] summarized the experimental and analytical investigations on the fluid and thermal environment in the gaps of control surface of the space shuttle. He concluded that continued research that includes more realistic three-dimensional (3D) flow and geometric effects is required to establish a firm database for the design of future high-speed vehicles. Wong and Kremer[14] performed a comprehensive two-dimensional (2D) numerical analysis to estimate the heating environment in the X-38 rudder–fin gap. The effects of gap shapes, real gas, radiation, Mach number, grid size, and turbulence were included in this research. It is found that unbearable heating occurred near the gap entrance and a seal[15] might be required to prevent excessive local heat flux on the structure. Alviani et al.[16–18] performed computational analysis of the flow near the cove regions of a high-speed swept wing–elevon model and found that separations were easily produced around the wing–elevon junction and the concomitant vortices produced streaks of high heat flux on the wing's surface. It is concluded that the highest levels of heat flux are on the leading-edge of the wing for the cove configuration.[16–18]

The mounting gap is another common type of surface imperfection that is defined as the region between the rudder and fuselage to accommodate the structural thermal expansion caused by the long-time aero-heating. The flow in the mounting gap is extremely complex for it is likely to undergo separation and curve or curl itself to create several vortices under the influence of wall shear stress and rudder-induced adverse pressure gradient. As a result, the aero-heating in the mounting gap is extremely severe, no less than the thermal environment experienced by the leading edge of the wing. Meanwhile, there is a strong coupling between the flow inside and outside the gap, which may affect the aerodynamic and control performance of the rudder. Therefore, it is of great significance to understand the physics of flow in the rudder gap for the design of a TPS and control performance of the rudder. Previous studies on the rudder gap were primarily focused on the distribution characteristics of heat flux near the rudder shaft.[19] Winkelmann[20] conducted experiments to measure heat flux in the fin/body interference region with and without gaps at the early stage. Neumann and Hayes[21] experimentally studied the effect of rudder deflection angles and mounting gaps on missile surface heating. They identified that two possible types of flow separation may occur upstream of the cylinder via the results of oil flow. The patterns of separation in the mounting gap would switch from one to another at a critical gap height and a noticeable decrease in heat flux occurs accompanying this switch. This series of experiments were recently replicated by Alviani et al.[22] and Fano et al.,[23] consistent conclusions as the experiments were drawn, and more information about flow structures and aero-heating distributions were given. The results presented by Alviani et al.[22] showed that flow separation in the gap caused spike of heat transfer as large as 30 times the baseline level near its reattachment point located very close to the cylinder. In addition to the regions under the fin and upstream of the rudder on the fuselage found by Neumann in the experiments, Alviani et al. proposed that the upstream side of the rudder's surface is another region that should be focused on in the design of a TPS. The numerical results presented by Fano et al.[23] indicated that the simulated maximum heat transfer rate is larger than the experimental value and closer to the cylinder rudder than the closest thermocouple in the tunnel tests. Li et al.[24] investigated the aero-heating of the rudder shaft in the wind tunnel tests under two different flow regimes,

i.e., laminar and turbulent. The results indicated that the heat flux on the rudder shaft in the laminar flow is higher than that in the turbulent flow. Combined with numerical simulation, it was concluded that this result is caused by the difference of boundary layer thickness and velocity distribution entering the gap. Other experimental and numerical studies by Zhang et al.[25] showed that zones of high heat flux are mainly related to the reattachment of vortices and flow stagnation, and the increase of gap height leads to stronger gap overflow and horseshoe-type vortices around the rudder shaft.

The short literature review provided earlier shows that 3D flow separations and the occurrence of evolution and breakdown of vortices in the mounting gap directly relates to the extremely hostile distribution of heat flux in the gap. However, to the best of our knowledge, no earlier studies have intensively investigated the 3D separations and vortices in the rudder mounting gap. The primary focus of this study is to represent the detailed flow patterns in the mounting gap and investigate the mechanisms of extreme heat flux generated around the rudder shaft. In this work, the structures of vortices formed around the rudder shaft are depicted as a function of h/δ. We also take a closer look at the effect of vortex behavior on the distributions of heat flux on the rudder shaft and fuselage. Through our research, the connection between the generation of vortices and the production of extreme heat flux around the rudder shaft is clearly revealed. This study has significant implications for the understanding of complex flow in this disturbance region. The remainder of this article is organized as follows: Modeling, numerical methods, and convergence study are presented in Sec. II. Section III focuses on the results and discussion. Concluding remarks are provided in Sec. IV.

II. METHODOLOGY

A. Model and boundary conditions

The model simulated in this article is shown in Fig. 1. A swept rudder with a blunt leading edge is mounted on a flat plate by a rudder shaft. The rudder has a total length of 387 mm, height of 120 mm, radius of rudder leading edge (RLE) of 2.5 mm, and a sweep angle of 54°. The root thickness of the rear segment of the rudder is 60 mm, with an expansive angle from the RLE to the root. The position of the rudder shaft is 176.5 mm away from the apex of the swept rudder, and the radius of the rudder shaft is 36 mm. Variations of gap height are achieved by adjusting the height of the shaft. Assuming that the flow is symmetric about the symmetry plane, only interference flow field around the mounting gap of half model is simulated to save
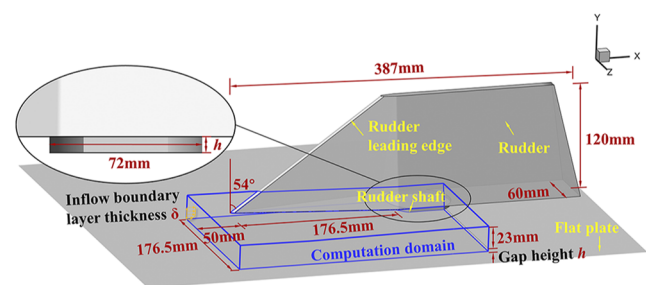

FIG. 1. Schematic of model and computation domain.

computation time and resources. As shown in Fig. 1, the computation domain has a total length of 282 mm, a width of 176.5 mm, and a total height of 23 mm with the gap height h. For example, the total height of the computation domain is 27 mm when the height of the mounting gap is 4 mm. The apex of the RLE is 50 mm away from the inlet of the computation domain. A separate 2D simulation of flat plate is carried out at Mach number (M_∞) of 10 with a static pressure (P_∞) and temperature (T_∞) of 3670.134 Pa and 220 K. The Reynolds number at this condition is 1.2×10^7 m^{-1}. In this case, a fully turbulent boundary layer develops along the plate. The velocity profile developed on the plate is extracted and is given as properties of input in the 3D simulations, assuming that the incoming flow is uniform in the z direction (see Fig. 1 for the coordinate direction). In this paper, the thickness of the extracted boundary layer is 7 mm. Simulations are carried out at different gap height ratios by varying the heights of the gap. Eight typical cases of them are chosen and discussed in this paper. The corresponding dimensionless gap height ratio h/δ varies from 0 to 1.42.

The boundary conditions adopted for the present study are set as follows: The left boundary of the computation domain is set as inlet, and the flow parameters are given based on the previous plate simulation. Top, right, and front boundaries are set as outflow. The boundary on the side of the symmetrical plane of the rudder is treated as symmetry plane. Non-slip and isothermal conditions are used for the solid walls at a fixed temperature of 298 K.

B. Numerical approach

Three-dimensional (3D) compressible Reynolds-averaged Navier–Stokes (RANS) equations are used in this study. It has been proved[26] that the distributions of surface friction lines (SFL) can be predicted well by RANS simulations for it is the result of the balance between the pressure and laminar viscous stress at the wall surface. These equations are written in dimensionless form as

$$\frac{\partial \mathbf{Q}}{\partial t} + \nabla \cdot (\mathbf{E}_e - \mathbf{E}_v) = 0, \tag{1}$$

where $\mathbf{Q}$ is the dependent variable vector, $\mathbf{Q} = [e \ \rho \ \rho u \ \rho v \ \rho w]^{\mathrm{T}}$, the inviscid flux vectors $\mathbf{E}_e$, and viscous flux vectors $\mathbf{E}_v$ are given as

$$\mathbf{E}_e = \begin{Bmatrix} (e+p)\mathbf{v} \\ \rho\mathbf{v} \\ \rho u\mathbf{v} + p\hat{\imath}_x \\ \rho v\mathbf{v} + p\hat{\imath}_y \\ \rho w\mathbf{v} + p\hat{\imath}_z \end{Bmatrix} \quad \mathbf{E}_v = \frac{1}{Re}\begin{Bmatrix} \beta_j\hat{\imath}_j \\ 0 \\ \left(\tau_{xj}^\ell + \tau_{xj}^t\right)\hat{\imath}_j \\ \left(\tau_{yj}^\ell + \tau_{yj}^t\right)\hat{\imath}_j \\ \left(\tau_{zj}^\ell + \tau_{zj}^t\right)\hat{\imath}_j \end{Bmatrix}, \tag{2}$$

where $\mathbf{v} = [u v w]^{\mathrm{T}}$; e is the total energy; ρ is the density; and u, v, and w are the velocity components in the x, y, and z directions, respectively. The shear-stress tensor is defined as

$$\tau_{ij}^\ell = \mu_\ell\left[\left(\frac{\partial u_i}{\partial x_j} + \frac{\partial u_j}{\partial x_i}\right) - \frac{2}{3}\frac{\partial u_k}{\partial x_k}\delta_{ij}\right], \tag{3}$$

where u_i are the Cartesian velocity components and x_i are the Cartesian coordinates. The viscous force work and heat transfer form,

β_i, is defined as $\beta_i = \tau_{ij}u_j - q_i$, where the heat transfer component is defined as

$$q_j = -\gamma\left(\frac{\mu_\ell}{\mathrm{Pr}} + \frac{\mu_t}{\mathrm{Pr}_t}\right)\frac{\partial(e_i)}{\partial x_j}. \tag{4}$$

The molecular dynamic viscosity coefficient, μ_ℓ, is computed by the Sutherland law.[27] The equation of state is given as $p = \rho RT$ or $e = \frac{p}{\gamma-1} + \frac{1}{2}\rho(u^2 + v^2 + w^2)$, where $\gamma = \frac{C_P}{C_V}$ and $R = C_P - C_V$. The turbulence effect is included by the Reynolds-stress tensor in the RANS equations, which is defined as

$$\tau_{ij}^t = \overline{u_i u_j}. \tag{5}$$

In this study, two-equation realizable $k - \varepsilon$ model (RKE)[28] is implemented to model the turbulence. The Reynolds-stress tensor is obtained from the modeled eddy viscosity (μ_t) and the available mean-strain tensor,

$$\rho\overline{u_i u_j} = \frac{2}{3}\delta_{ij}\rho k - \mu_t S_{ij}, \tag{6}$$

where

$$S_{ij} = \left(\frac{\partial u_i}{\partial x_j} + \frac{\partial u_j}{\partial x_i} - \frac{2}{3}\frac{\partial u_k}{\partial x_k}\delta_{ij}\right). \tag{7}$$

Two extra transport equations, one for the evolution of k and one for ε, are added to the equation system, shown as

$$\frac{\partial(\rho k)}{\partial t} + \frac{\partial}{\partial x_j}(u_j\rho k) = \frac{\partial}{\partial x_j}\left[\left(\mu_\ell + \frac{\mu_t}{\sigma_k}\right)\frac{\partial k}{\partial x_j}\right] + P_k - \rho\varepsilon, \tag{8}$$

$$\frac{\partial(\rho\varepsilon)}{\partial t} + \frac{\partial}{\partial x_j}(u_j\rho\varepsilon) = \frac{\partial}{\partial x_j}\left[\left(\mu_\ell + \frac{\mu_t}{\sigma_\varepsilon}\right)\frac{\partial\varepsilon}{\partial x_j}\right] + (C_{\varepsilon 1}P_k - C_{\varepsilon 2}\rho\varepsilon + E)T_t^{-1}. \tag{9}$$

In which the rate of production of turbulence energy $P_k = -\rho\overline{u_i u_j}\partial u_i/\partial x_j$, T_t is a realizable estimate of the turbulence timescale

$$T_t = \frac{k}{\varepsilon}\max\{1, \zeta^{-1}\}, \quad \zeta = \sqrt{R_t/2}. \tag{10}$$

R_t is the turbulence Reynolds number, $R_t = \rho k^2/(\mu_\ell\varepsilon)$. The addition term E is designed to improve the model response to adverse pressure-gradient flows. This term has the following form:

$$E = A_E\rho\sqrt{\varepsilon T_t}\Psi\max\left\{k^{\frac{1}{2}}, (v\varepsilon)^{\frac{1}{4}}\right\}, \quad \Psi = \max\left\{\frac{\partial k}{\partial x_j}\frac{\partial\tau}{\partial x_j}, 0\right\}, \tag{11}$$

$$\tau = k/\varepsilon.$$

Constants are given as $C_\mu = 0.09, C_{\varepsilon 1} = 1.44, C_{\varepsilon 2} = 1.92, \sigma_k = 1.0, \sigma_\varepsilon = 1.3$, and $A_E = 0.3$.

The modeled eddy viscosity μ_t is obtained from

$$\mu_t = \min\left\{C_\mu f_\mu\rho k^2/\varepsilon, 2\rho k/3S\right\}. \tag{12}$$

S is the dimensional strain magnitude and f_μ is a low-Reynolds number function, designed to account for viscous and inviscid damping of turbulent fluctuations in the proximity of solid surface,

$$f_\mu = \frac{1 - \exp^{-0.01R_t}}{1 - \exp^{-\sqrt{R_t}}} \max\left\{1, \left(\frac{2}{R_t}\right)^{\frac{1}{2}}\right\}. \tag{13}$$

In this work, the discretization of the 3D compressible Reynolds-averaged Navier–Stokes (RANS) equations is based on a quadrilateral-grid-based finite-volume method. The convective flux discretization is accomplished by the non-linear Harten–Lax–van Leer contact (HLLC) scheme, which can define interface fluxes with entropy and positivity conditions satisfied automatically. Second-order accuracy for the spatial discretization can be obtained by a total variation diminishing (TVD) scheme with a new multi-dimensional polynomial interpolation with the use of nodal polynomials. The continuous limiter is employed to suppress spurious oscillations near the discontinuities. An approach based on face polynomials is used to approximate the viscous fluxes. The time integration is performed by a second-order fully implicit scheme. This computational code has been used and validated in the previous work by Peng et al.,[29] Zhang et al.,[30] and Lu et al.,[31] showing excellent performance in solving hypersonic flows, including shock interactions, boundary layer separations, and shock-induced combustion.

C. Code validation

A shock-wave/turbulent-boundary-layer interaction case induced by the 3D sharp fin is utilized to verify the ability of computation of the present code. The experimental data of LF23,[32] together with the available results of RANS simulation[33] that used Negative Spalart-Allmaras (SA-NEG) turbulence model, are taken for comparison with our numerical results. The simulation initial conditions are p_∞ = 4009.048 Pa, T_∞ = 68.33 K, M_∞ = 5, and $Re/\text{m} = 37 \times 10^6$ m^{-1}. Solid walls are treated as isothermal surface with a fixed temperature of T_w = 300 K. Figure 2(a) shows pressure distributions nondimensionalized by freestream pressure at the streamwise location x = 0.153 m; Fig. 2(b) shows comparisons of measured skin friction and simulation from reference computational fluid dynamics (CFD) with present results. The distributions of surface heat flux at z = 0.121 m are represented
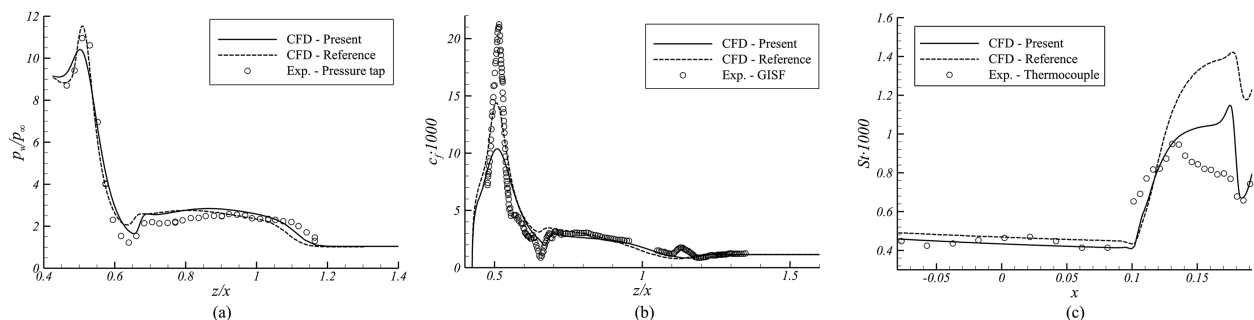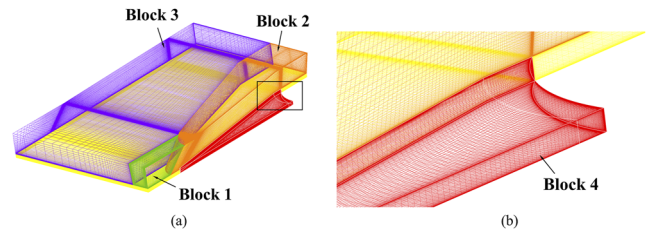

FIG. 3. Generated 3D structural mesh employed in this study, and the XOY plane is the symmetric plane. (a) The whole grid system and (b) grids near the rudder shaft.

with its dimensionless form, i.e., Stanton number, as shown in Fig. 2(c). As shown in Fig. 2, the overall trend of aerodynamic loads can be rebuilt by our computation, indicating well capacities of the numerical solver used in this paper to capture the typical structures of flow field and distribution trend of surface aerodynamic loads. Although the prediction size and position of the separation vortex were unsatisfactorily precited by the present code, which leads to the discrepancy in Figs. 2(b) and 2(c), the occurrence and influence of the separation vortex on the aerodynamic parameters were well predicted. RANS inevitably has some limitations in handling separation because it is the result of time averaging of vortex structures. However, the result can be obtained in a short time, and the characteristics of flow field structure can be seen. The large separated vortex caused by boundary layer separations, which is the main concern in this paper, can also be captured. From the perspective of engineering application, RANS is obviously superior to direct numerical simulation (DNS) or large eddy simulation (LES)—the latter takes a lot of computational resources to deal with the small pulsating vortex structures in the boundary layer.

D. Convergence study

Mesh generation obeys the following strategy: First, generate the mesh of rudder without mounting gap, which is composed of three blocks (block 1–3) shown in Fig. 3. Then, extrude the lower surface of the existing grids along the negative y direction to generate the remaining mesh, which is the mesh of the mounting gap labeled block 4 in Fig. 3. The details of the computation domain are given

FIG. 2. Comparison of distributions of wall pressure ratios along the plate at x = 0.153 m (a), skin friction along the plate at x = 0.122 m (b), and heat flux along the plate at z = 0.121 m (c) for LF23 case obtained by reference CFD,[33] experiment,[32] and present code (unit: m).

TABLE I. Details of the computation domain.

| Gap height ratio h/δ | Gap mesh N_Y | Mesh of rudder without mounting gap ($N_X \times N_Y \times N_Z$) | | | Total cells |
		Block 1	Block 2	Block 3	
0	0				2.76×10^6
0.07	50				5.91×10^6
0.28, 0.5, 0.64	75	$47 \times 59 \times 75$	$376 \times 59 \times 81$	$348 \times 59 \times 42$	7.51×10^6
0.85, 1.13	100				9.19×10^6
1.42	125				10.72×10^6

in Table I. The height of the first cell near the solid wall is kept as 1×10^{-3} mm to ensure the value of $y+$ is less than 1. As far as numerical results are concerned, it is worth noting that all the CFD results provided in the paper refer to both converged and grid independent computations. Grid convergence study is performed on three resolutions of mesh for $h/\delta = 0.5$. The details of domains are given in Table II. The grid is encrypted primarily in the gap, namely, block 4, to make the best use of the additional grid points. Figure 4 shows the results of the grid independence study. Q_{ref} is the undisturbed heat flux on the fuselage. It can be seen from Figs. 4(a) and 4(c) that the distributions of pressure and heat flux have shown good convergence with the increase in mesh density. There are some deviations in the distributions of c_f [see Fig. 4(b)], which is hard to avoid[22] at the grid resolution that currently use. The main content of this paper is the topological connections of the SFL, which depends on the variation trend of c_f, instead of specific values. The resolution of grid currently used can meet the requirements. To save computational cost without compromising accuracy to a large extent, the

middle grid is chosen for the present study. In order to assess the numerical solution convergence, the density equation residual and aerodynamic coefficients are monitored during the iterations. Solution convergence is assumed when normalized residual drops more than three orders of magnitude and the aerodynamic coefficients do not vary anymore or oscillate in a small range with a fixed period.

III. RESULTS AND DISCUSSION

In this section, the flow field properties in the rudder gap are evaluated numerically. Particularly, the discussion of complex flow structures in the mounting gap is primary based on the topological properties of surface limiting streamlines [i.e., surface friction lines (SFL)] and volume streamlines. Surface friction lines are composed of vectors of wall shear stress in viscous flow, which can be obtained easily by oil flow techniques in the wind tunnel experiments. The significance of skin friction is that it is the key to reconstruct near-wall structures together with surface pressure.[34,35] The distributions

TABLE II. Grid convergence parameters for $h/\delta = 0.50$.

| | Mesh of rudder without mounting gap ($N_X \times N_Y \times N_Z$) | | | Gap mesh ($N_X \times N_Y \times N_Z$) | First cell thickness (mm) | Total cells |
	Block 1	Block 2	Block 3	Block 4		
Coarse	$47 \times 59 \times 50$	$276 \times 59 \times 81$	$273 \times 59 \times 42$	$150 \times 50 \times 50$	2×10^{-3}	4.14×10^6
Middle	$47 \times 59 \times 75$	$376 \times 59 \times 81$	$348 \times 59 \times 42$	$225 \times 75 \times 75$	1×10^{-3}	7.51×10^6
Fine	$47 \times 59 \times 100$	$476 \times 59 \times 81$	$423 \times 59 \times 42$	$300 \times 100 \times 100$	1×10^{-3}	12.33×10^6
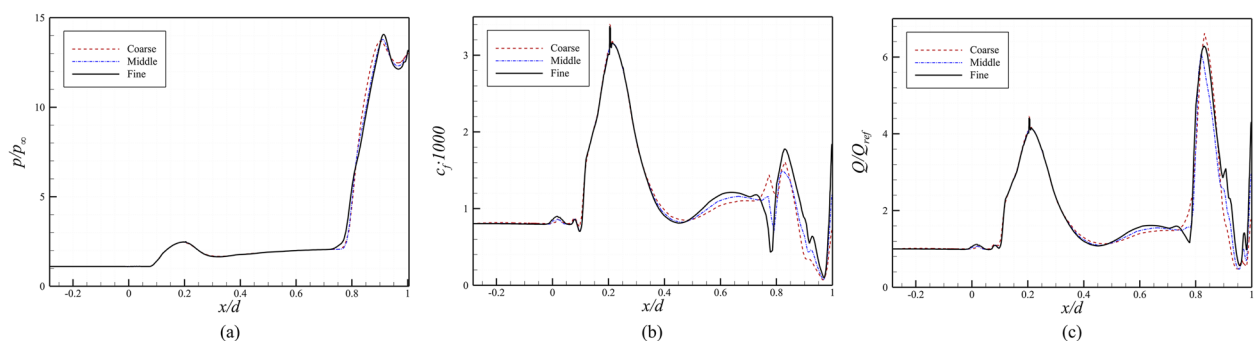
FIG. 4. Distributions of pressure (a), skin-friction coefficient (b), and heat flux (c) computed by three different mesh resolutions at the surface of the wall.
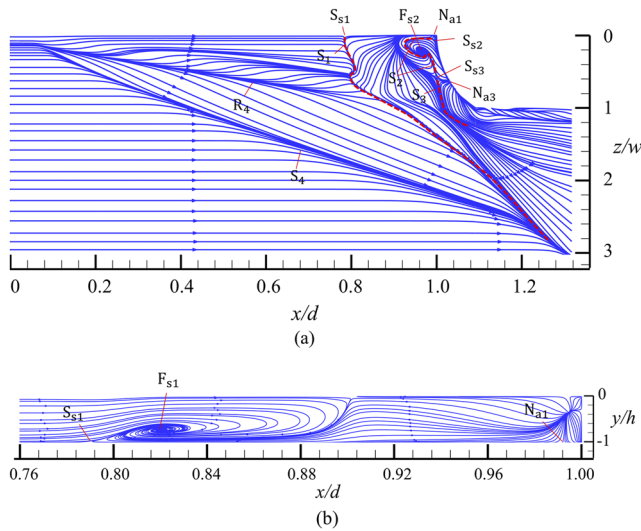
FIG. 5. Overall distribution of SFL on the fuselage (a) and streamlines in the symmetry plane (b) at $h/\delta = 0.50$.

of SFL contain distinct topological features, such as critical points and lines of separation and attachment, which reveal near-wall structures of complex flows.[36] The topological approach is based on the idea of Poincaré[37] and was first implemented in the study of separated flow by Legendre[38] and Lighthill.[39] After more than 60 years of development, the theory of critical point[40] and topological notations have provided a framework for investigation on 3D flows.[41,42] Many studies[26,43–55] have utilized distributions of SFL and topological notations to study complex flow structures of 3D separated flow.

This section is organized as follows: First, in Secs. III A and III B, the types of 3D separation and flow conditions for two gap height ratios, namely, h/δ = 0.50 and 0.85, are studied, and the mechanisms of extreme heat transfer distributions are analyzed. In Sec. III C, the effects of increasing the gap height ratios on the flow topology and distributions of extreme heat flux are discussed.
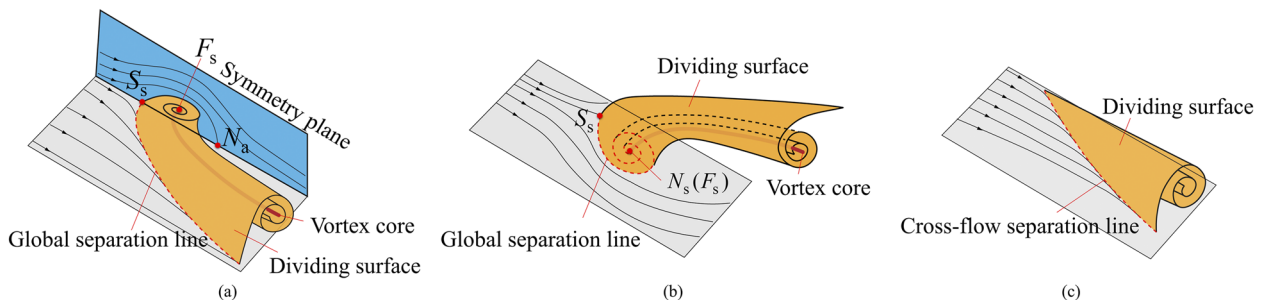
A. Flow field properties of h/δ = 0.50

In this section, we describe in detail the topology of SFL on the fuselage [Fig. 5(a)] and streamlines in the symmetry plane [Fig. 5(b)] to identify the types of 3D separation occurring in the mounting gap. Along the centerline ($z/w = 0$), a saddle S_{s1} is located upstream of the rudder shaft, from where the primary separation line S_1 is originated. There is an attachment nodal point N_{a1} near the root of the rudder shaft [see Fig. 5(a)] and an additional spiral node F_{s1} in the flow field [see Fig. 5(b)]. The combination of S_{s1} and N_{a1} are associated with Type I separation, i.e., horseshoe vortex[41] [see Fig. 6(a)]. Behind the horseshoe vortex (vortex 1), there is a separation nodal point, focus F_{s2}, and both saddle points S_{s2} and S_{s3} divert flow into it. Due to Helmholtz's theorems of vorticity, a vortex tube cannot end within a fluid and the flow must lift off the surface.[43] The pairs of $S_{s2} - F_{s2}$ and $S_{s3} - F_{s2}$ indicate Type II separation[41] [see Fig. 6(b)]. Since the pattern of vortex of this type of separation resembles a tornado, we refer it as a tornado-type separation[49] (vortex 2) in this article. In addition, an attachment nodal point N_{a3} locates very near to the juncture of the fuselage and rudder shaft [see Fig. 5(a)]. It acts as a source feeding in the saddle points S_{s2} and S_{s3}. The saddle–nodal pair of $S_{s2} - N_{a3}$ indicates a small horseshoe vortex (vortex 3), with a 3D spiral node F_{s3} in the flow (see slice 3 in Fig. 7). The separation line of this global separation is S_3.

An overview of direction of near-wall flow can be obtained by means of topological connections of singularities in the SFL of the surface. Originating from the attachment nodal point N_{a3}, a portion of the flow is drawn toward S_{s2} and roll around the central vortical core F_{s2} to form a tornado vortex. There is also a partial flow that directly gets sucked into F_{s2} after leaving N_{a3}. The other portion of flow moves along spanwise direction of the rudder shaft and separates at S_3, originating to a horseshoe vortex (vortex 3) attached to the side surface of the rudder shaft. The separation lines, shown as red dashed lines in Fig. 5, are known as global lines of separation characterized by isolating the upstream region from the downstream. The incoming flow is restricted at S_1 and separated from fuselage, curling downstream to form primary horseshoe vortex (vortex 1). The extent of flow originating from N_{a3} is limited by S_2 and S_3. The lines of global separation play the role of the base of the stream surfaces that are called dividing surfaces[43] according to Tobak and Peake.[56] Some authors also referred to such surfaces

FIG. 6. Schematic representation of the three-dimensional flow separation and formation of horseshoe vortex (a) and tornado-type vortex (b). Dividing surface formed from (a) combinations of separation saddle point S_s and attachment nodal point N_a; (b) combinations of separation saddle point S_s and separation nodal point N_s, i.e., focus F_s; (c) particular SFL toward which adjacent SFL converges. There is no singular point in the distributions of SFL in this case (refer to Tobak and Peake[56]). (a) Type I separation. (b) Type II separation. (c) Cross-flow separation.
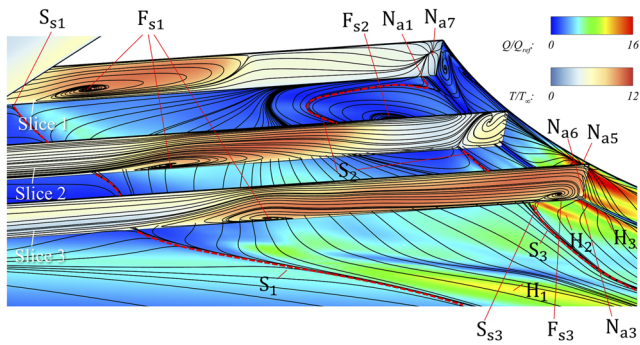
FIG. 7. Distributions of SFL on the fuselage and rudder shaft, with external streamlines shown in three streamwise slices, corresponding to the center span (z/w = 0 for slice 1) and two off-center spanwise locations (z/w = 0.36 and z/w = 0.64 for slices 2 and 3) at h/δ = 0.50. Distribution contours of temperature are shown in three streamwise slices, and the distributions of heat flux are superposed on the surfaces of the fuselage and rudder shaft.

as separation surfaces[41,42,44,46,47,57] because they originate from the lines of separation and divide the flow field away from the wall.[58] The terminology defined by Tobak and Peake[56] is utilized in this paper. In addition to global separations, there is a crossflow separation[41] [see Fig. 6(c)] characterized by a separation line S_4 to which all neighboring SFL converge asymptotically. In conclusion, the

topology of SFL on fuselage in front of the rudder shaft at h/δ = 0.50 (Fig. 5) results from the coexistence of a tornado-type vortex and two horseshoe-type vortices.

To further clarify the overall flow structures and get insight into the shapes and effects of 3D vortices in the mounting gap, patterns of streamlines and distributions of static temperature of the streamwise slices of flow field are extracted at three spanwise locations (z/w = 0, 0.36, and 0.64). Distributions of SFL and heat flux are also given on the surfaces of fuselage and rudder shaft, as shown in Fig. 7.

Consider the flow at spanwise z/w = 0, which is referring to slice 1 in Fig. 7 with a zoomed-in view presented in Fig. 8(a). The topology in this plane can be drawn an analogy with the flow in the end-wall region of a surface-mounted obstacle,[59] which is commonly referred to as juncture flow. The incoming flow decelerates under the effect of adverse pressure gradient imposed by the rudder shaft. The boundary layer separates from the fuselage at separation line S_1 and originates to a primary horseshoe vortex (vortex 1), the stream surface of which stops high speed incoming flow from arriving at the rudder shaft. It can be seen in Fig. 8(a) that the flow at the center span is redirected by dividing surface 1 on its way toward the rudder shaft and trapped in the horseshoe vortex 1 as it propagates downstream. Most of the fluid in front of the rudder shaft is low-speed backflow with only very little at positive speed, the source of which is 3D singular point N_{a7}, corresponding to two-dimensional (2D) singularity N_{a1} on the centerline of surface.
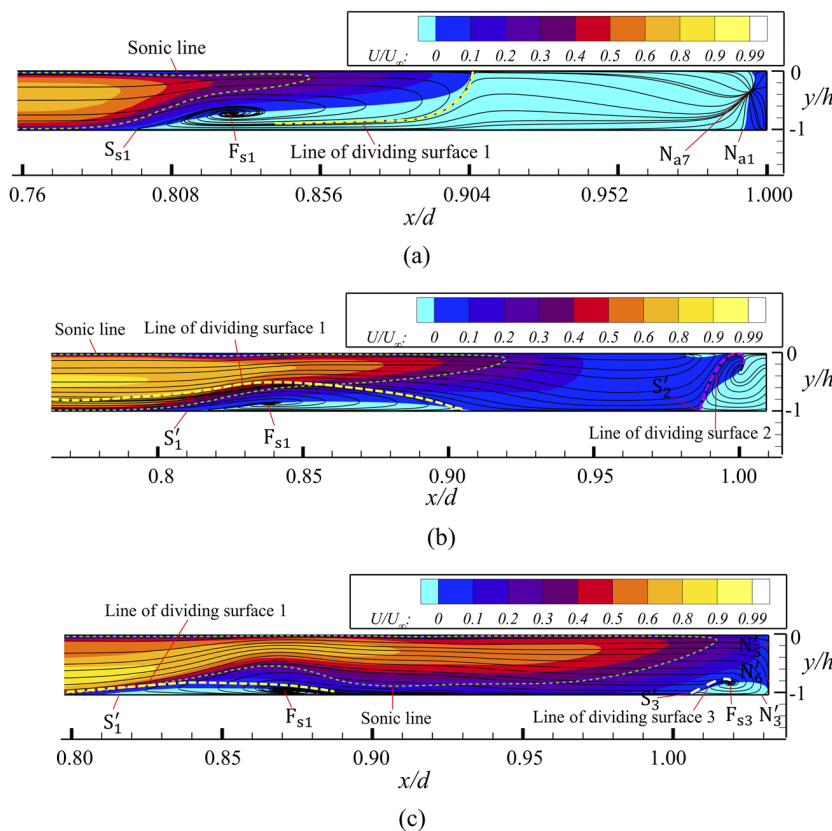

(a)

(b)

(c)

FIG. 8. Zoomed-in view of three streamwise slices of flow field at h/δ = 0.50 at spanwise z/w = 0 (a), 0.36 (b), and 0.64 (c), respectively, with the green dashed lines indicating sonic lines and yellow, purple, and white dashed lines showing how the stream surfaces are interwoven and stretched by the vortical structures[43] and isolate the flow from one side to another. (a) Streamwise slice of flow field at spanwise z/w = 0. (b) Streamwise slice of flow field at spanwise z/w = 0.36 (c) Streamwise slice of flow field at spanwise z/w = 0.64.

Consider the flow at spanwise z/w = 0.36, which is referring to slice 2 in Fig. 7 with the zoomed-in view presented in Fig. 8(b). The singularities in the slices of flow field are represented by the labels with superscript, and proceeding numbers of subscript are the same as the corresponding 3D singularities. It can be seen from Fig. 8(b) that the thickness of the primary horseshoe vortex (vortex 1) gradually deflates along the spanwise direction, resulting

in the barrier effect of dividing surface 1 against the incoming flow fails. However, due to the dividing surface of the tornado-type vortex, the flow at high kinetic cannot reach the rudder shaft even though it climbs over the vortex 1 at this time. As shown in slice 2 in Fig. 7, the incoming flow is sucked into the tornado-type vortex, rotates around the focus F_{s2}, and leaves the fuselage surface at the global separation line S_2 after overing vortex 1. In the streamwise slice shown in Fig. 8(b), the boundary layer of the fuselage separates at the separation points S_1' and S_2'.

Further moving along the spanwise direction, consider the flow at spanwise z/w = 0.64, which is referring to slice 3 in Fig. 7 with the zoomed-in view presented in Fig. 8(c). In this case, the incoming flow stagnates on the rudder shaft, producing high-pressure and high-heat-flux region on it. It can be seen from Fig. 7 that the backflow near the plane of symmetry is supplemented by this part of fluid. The flow decelerates and curls down in front of the rudder shaft to form horseshoe vortex 3 and will propagate along the negative and positive directions of z-axis, i.e., spanwise. The fluid moving along the z-direction, that is, the negative direction of the spanwise, enters vortex 1 and vortex 2, respectively.

By analyzing the distributions of limiting and volume streamlines, the structures of 3D vortices occurring in the rudder mounting gap can be visualized. They are displayed through 3D stream-traces in Fig. 9. The primary horseshoe vortex (vortex 1) is similar with a spindle [see Fig. 9(a)]. During its propagation around the rudder shaft, it expands slightly in the normal direction of streamwise and wall, then shrinks rapidly, as shown in Fig. 10. As the name suggests,
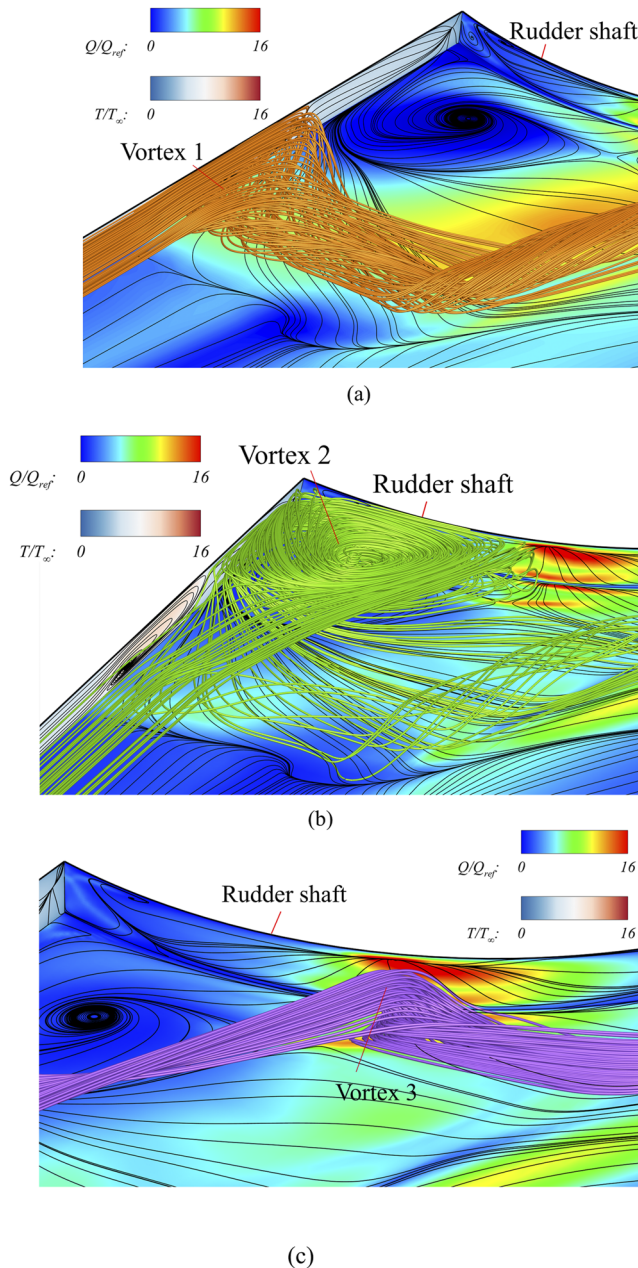

FIG. 9. Sketches of (a) primary horseshoe vortex (vortex 1), (b) tornado-type vortex (vortex 2), and (c) horseshoe vortex (vortex 3) attached to the rudder shaft occurring in the mounting gap at $h/\delta = 0.50$.
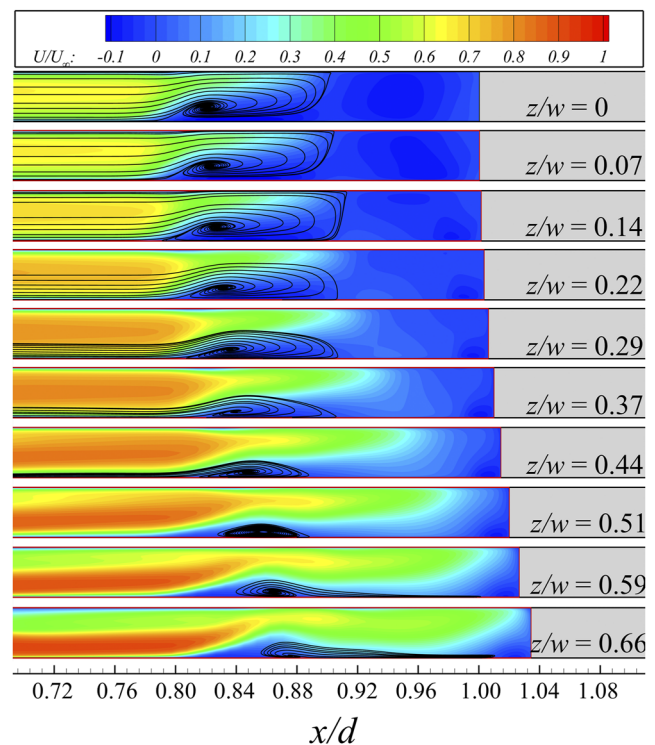

FIG. 10. Streamwise slices of primary horseshoe vortex (vortex 1) along different spanwise locations (z/w = 0–0.66) at $h/\delta = 0.50$.

vortex 2 is shaped like a tornado [see Fig. 9(b)]. It rotates around the vortex core originating from the focus F_{s2}, creating a low-pressure region in front of the rudder shaft and isolating the high-speed incoming flow. When the incoming high-speed flow is blocked by the rudder shaft and rolls down, vortex 3 forms [see Fig. 9(c)]. The scope of downward curl of vortex 3 decreases with the increase in position of spanwise (see Fig. 11), as the consequence of decrease of skewing of streamlines due to the presence of the surface-mounted rudder shaft.

It can be seen from Figs. 7 and 9 that the localized high heat flux on the rudder shaft is caused by the attached horseshoe vortex (vortex 3). This horseshoe vortex brings the fluid of high momentum nearer to the wall surface, which increases the velocity gradient normal to the wall and produces higher local skin friction. Therefore, the fluid at freestream temperature is transported closer to the wall surfaces by this vortex and produces regions of high localized heat flux.[60] The generation of regions of high aero-heating labeled H_2 and H_3 (see Fig. 7) in the juncture of the rudder shaft and fuselage are produced out of the same reason. In addition to H_2 and H_3, there is another region of high heat flux located at the entrance of the gap, marked as H_1 in Figs. 7 and 9. It is speculated that this area of high heat flux is related to the sudden thinning of the local boundary
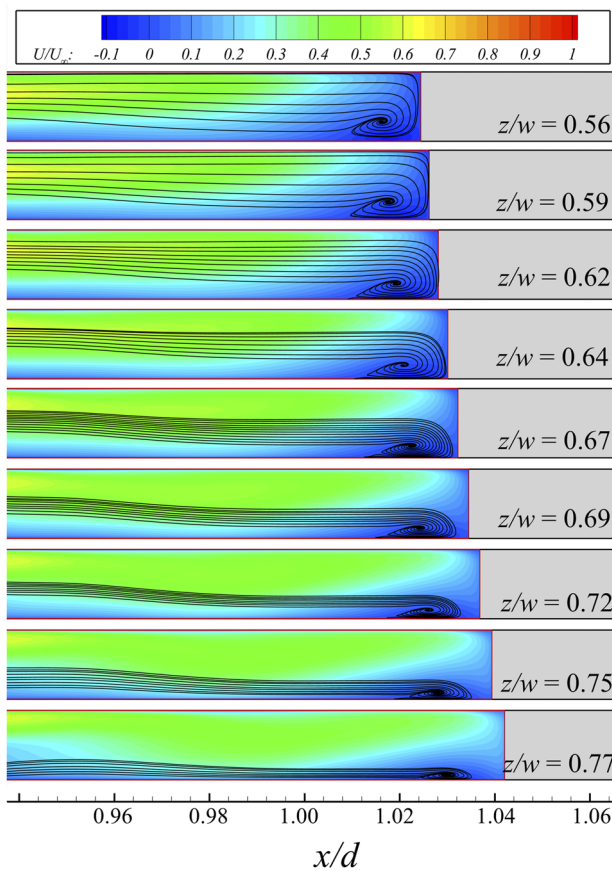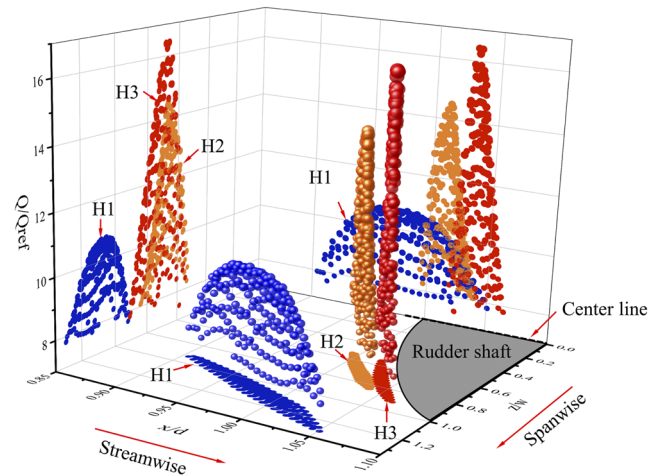

FIG. 12. The spatial distributions of three localized high heat flux regions of surface of fuselage in the directions of streamwise, spanwise, and wall normal at $h/\delta = 0.50$.

layer, which is caused by the transverse flow of high-pressure fluid behind the rudder shock to the region of lower pressure on both sides of it. The spatial distributions of three regions of high heat flux, labeled H_1–H_3, are presented in Fig. 12. The spheres colored blue, orange, and red represent the positions and values of points of high heat flux in the regions of H_1, H_2, and H_3 on the fuselage, respectively. We project them along the streamwise, spanwise, and wall normal direction, respectively, to show the spatial distributions of high heat flux. It is worth pointing out that the streamwise variation of heat flux is actually the superposition of localized high heat flux that occurs at different spanwise locations, and the spanwise
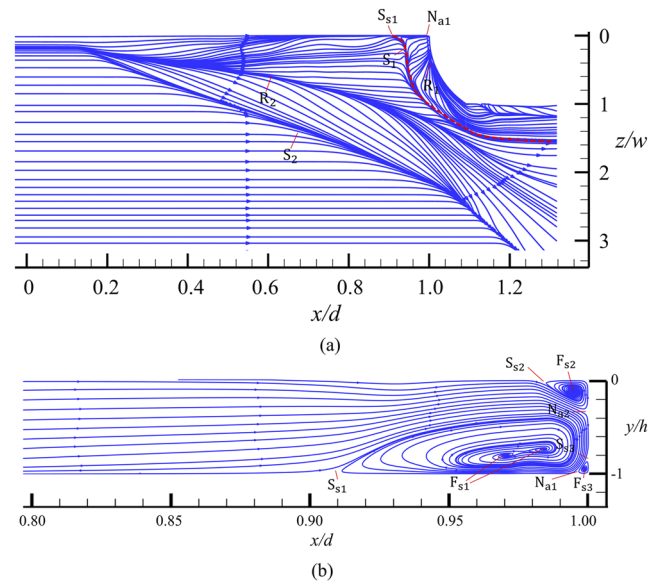

FIG. 11. Streamwise slices of horseshoe vortex attaching to the rudder shaft (vortex 3) along different spanwise locations (z/w = 0.56–0.77) at $h/\delta = 0.50$.

FIG. 13. Overall distribution of SFL on the fuselage (a) and streamlines in the symmetry plane (b) at $h/\delta = 0.85$.
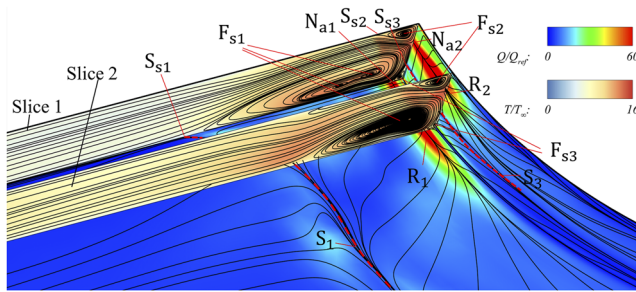
FIG. 14. Distributions of SFL on the fuselage and rudder shaft, with external streamlines shown in two streamwise slices, corresponding to the center span (z/w = 0 for slice 1) and off-center spanwise location at z/w = 0.15 at h/δ = 0.85. Distributions of contours of temperature are shown in two streamwise slices, and the distributions of heat flux are superposed on the surfaces of the fuselage and rudder shaft.

variation is also similar to the streamwise. Since both H_2 and H_3 are related to the formation of horseshoe vortex 2, their spanwise locations are basically identical in the region of z/w = 0.55–0.85. As the center of the rudder shaft is occupied by backflow, the maximum value of localized heat flux is not located near the centerline in the direction of spanwise, but approximately near half of the rudder shaft at z/w = 0.6, which is produced by the horseshoe vortex 2.

B. Flow field properties of h/δ = 0.85

When the gap height ratio h/δ increases from 0.5 to 0.85, the topology of SFL on the fuselage changes significantly with the indication of transition of types of three-dimensional (3D) separation occurred in the mounting gap. The overall distribution of SFL on the fuselage, shown in Fig. 13, has the characteristics of a classical 3D boundary layer separation with a combination of saddle–nodal points located upstream of the rudder shaft. Global separation line S_1 and reattachment line R_1 wrap around the rudder shaft.[59] In the case of h/δ = 0.85, there is only one type of 3D global separation, i.e., type I separation [see Fig. 6(a)], taking place in the mounting gap as a result of the absence of foci in the SFL on the fuselage. In addition to the primary horseshoe vortex, the strong convergence of SFL at S_2 indicates a crossflow separation [see Fig. 6(c)] due to the interference of rudder shock wave with the boundary layer of fuselage. The streamlines in the symmetry plane [Fig. 13(b)] show a system of three vortices upstream of the rudder shaft. Except for the primary horseshoe vortex 1, two counter-rotating structures, vortex 2

and vortex 3 [see Fig. 13(b)], are established in the upper and lower junctures of the rudder shaft due to the separations of boundary layers of the lower surface of the rudder and the leading surface of the rudder shaft, respectively.

It can be observed from Fig. 14 that as the mounting gap ratio h/δ increased to 0.85, the incoming flow can arrive at and create a region of localized high heat flux at the centerline of the rudder shaft. Footing on the global lines of separation, dividing surfaces 1–3 prefer rolling up to form the familiar coiled sheet around the center vortical cores F_{s1}, F_{s2}, and F_{s3} rather than separating flow from one side to another (see Fig. 15). When approaching the rudder shaft, the fluid separates and forms three main vortices, namely, vortices 1, 2, and 3, as shown in Fig. 16. Most of the fluid is entrained by the primary horseshoe vortex (vortex 1). The fluid above the stream surface that attaches at the line of attachment R_2 forms a juncture vortex 2 under the entrainment of curl of dividing surface 2. There is a smaller juncture vortex 3 in the juncture formed by the rudder shaft and the fuselage, dividing surface of which prevents fluid in the juncture entering the primary horseshoe vortex 1.

Different from the case at h/δ = 0.50 of which the locations of regions of localized high heat flux are on the side of the rudder shaft, extreme heat flux distributes near the centerline of the rudder shaft at h/δ = 0.85, as shown in Fig. 17. The region of high heat flux labeled H_1 is related to the global separation of the boundary layer of the fuselage at the line of separation S_1, while H_2 is caused as a result of the fluid at the freestream temperature being transported near the fuselage surface at the line of attachment R_1 by primary horseshoe vortex 1. It can be seen from Fig. 17 that the maximum value of heat flux is located at the centerline of the rudder shaft when the incoming flow at the symmetry can reach the rudder shaft.

C. Effect of gap height ratios

The effect of gap height ratios h/δ on the types of three-dimensional (3D) separation and distributions of extreme heat flux is explored in this section. The maximum values of heat flux on the surfaces of fuselage and rudder shaft at different gap height ratios are shown in Fig. 18, with the distributions of SFL on the surface of the fuselage [Fig. 18(a)] and streamlines in the symmetry plane [Fig. 18(b)] presenting the flow characteristics given at different h/δ.

The types of 3D separation appeared in the mounting gap change significantly with the increasement of gap height, as can be seen from the distributions of SFL on the fuselage in Fig. 18(a). For the h/δ = 0.07 case, the incoming flow enters the gap at a relatively low velocity and basically blocked. At this point, the thermal environment in the gap is almost the same as the case without a
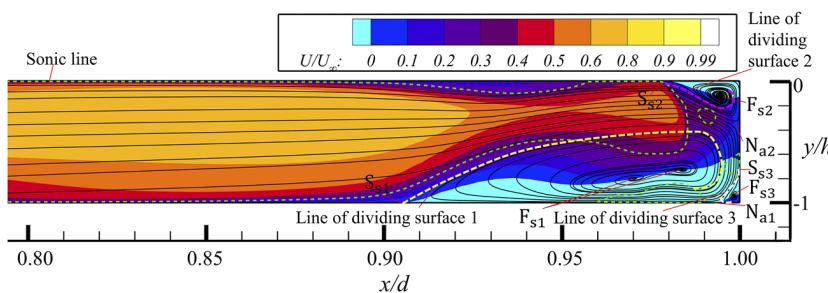

FIG. 15. Zoomed-in view of the streamwise slice of flow field at h/δ = 0.85 at spanwise z/w = 0 with the green dashed lines indicating sonic lines.
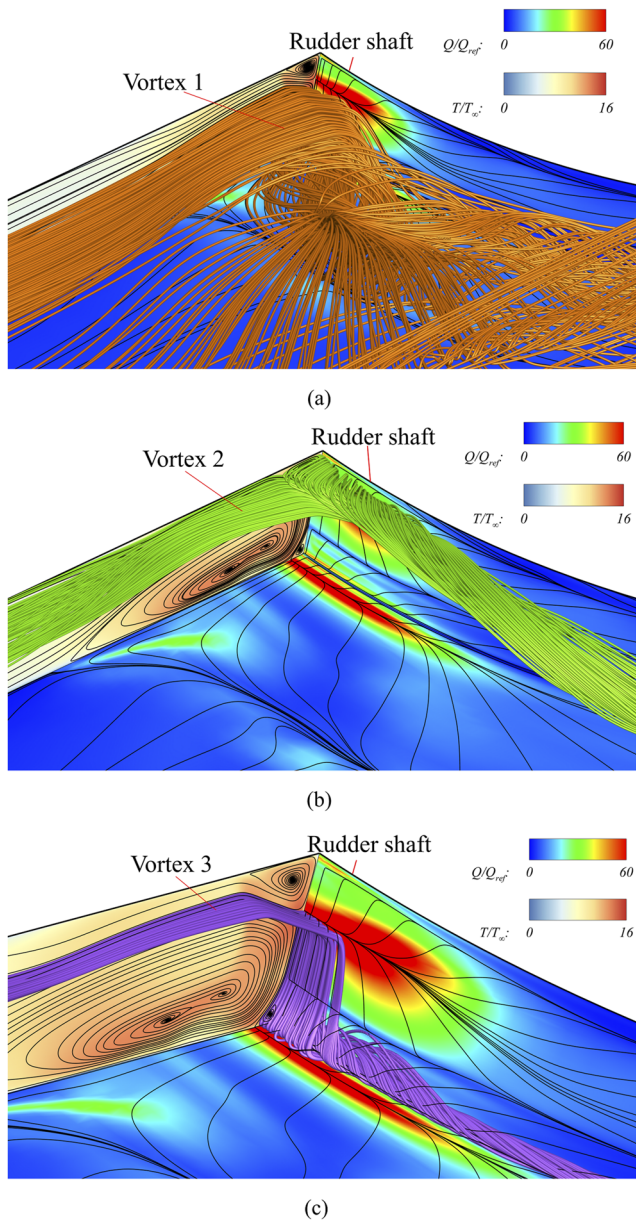
FIG. 16. A sketch of the three vortices occurring in the mounting gap at $h/\delta = 0.85$. (a) Schematic of the primary horseshoe vortex (vortex 1). (b) Schematic of the upper-juncture vortex (vortex 2). (c) Schematic of the lower-juncture horseshoe vortex (vortex 3).
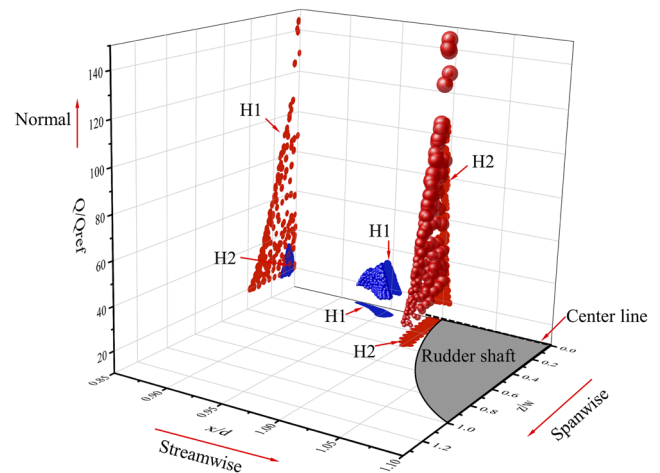

FIG. 17. The spatial distributions of two localized high heat flux regions of surface of fuselage in the directions of streamwise, spanwise, and wall normal at $h/\delta = 0.85$.

mounting gap ($h/\delta = 0$). As the gap height ratio increases, high-speed fluid enters the gap and experiences both type I and type II of global 3D separation [Figs. 6(a) and 6(b)]. The fluid forms horseshoe vortices and tornado-type vortices around the rudder shaft. As mentioned earlier, the production of extreme heat flux around the rudder shaft is closely related to the high-momentum flow transported toward the wall surface by the horseshoe vortex. It is also

found in this paper that the tornado-type vortex can barrier high-momentum fluid from reaching the rudder shaft and, thus, prevents its direct stagnation on the surface of the rudder shaft to create extreme high heat flux. As shown in Fig. 18(a), when the gap height ratio is less than 0.85, there is a focus in the SFL, indicating the existence of tornado-type vortex in the flow field.[40,51,61] The tornado has the effect of pulling the high-speed incoming flow away from the rudder shaft. As a result, the area directly in front of the rudder shaft is occupied by low-speed backflow, and the regions of high heat flux of fuselage are distributed on the side of the rudder shaft with a relatively small magnitude. When the gap height ratio further increases to greater than 0.85, the fluid at nearly freestream temperature and velocity [see Fig. 18(b)] reaches the rudder shaft and generates extremely high localized heat flux on the surface of fuselage and rudder shaft at the centerline. Therefore, $h/\delta = 0.85$ can be regarded as the critical gap height around which the patterns of vortices in the gap changed. Neumann and Hayes[21] revealed that a noticeable drop in surface heating occurred at the critical gap height, which is supported by the decrease of heat flux presented in Fig. 18.

In general, the regions of localized high heat flux on the fuselage and rudder shaft gradually move from the side to the center of the rudder shaft with the improvement of magnitude of maximum values, as the gap height ratio varies from 0 to 1.42. The most severe local thermal environment occurs when $h/\delta = 0.85$, in which case the flow separation occurred very close to the rudder shaft. There is a puzzle on the cause of the nearest location of separation occurred to the rudder shaft at $h/\delta = 0.85$, which may be the result of the evolution of multi-vortex system in front of the finite height obstacles.[59] When the gap height is comparable to the incoming boundary layer, that is, the gap height ratio is around 1, the aforementioned two configurations share many characteristics. More research is needed to investigate the cases when the gap height ratio is around 1, which is not the main focus of this paper. It can be seen from Fig. 18(b) that, while the gap height increases further, flow separation occurs earlier along the centerline, but the consequent separation bubble occupies
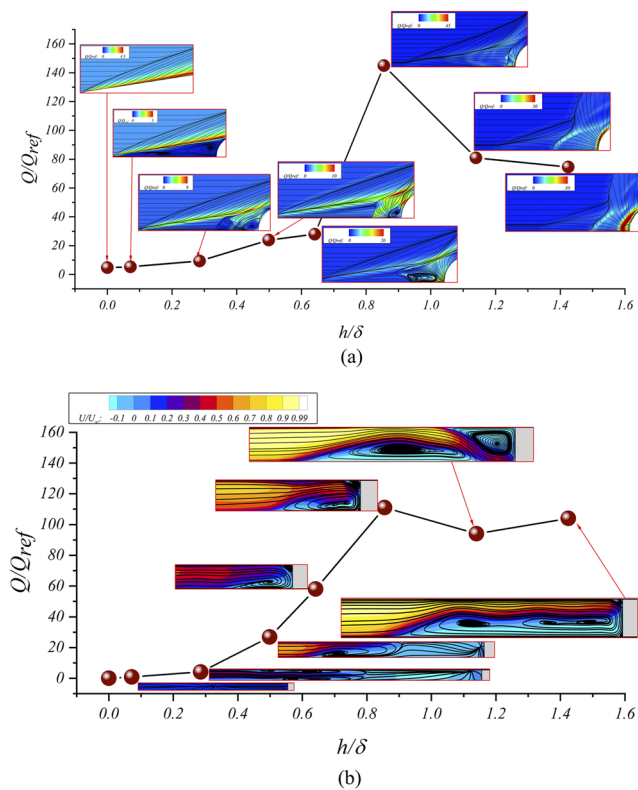
FIG. 18. Effect of gap height ratios on the distributions of extreme heat flux. (a) Maximum values of heat flux on the fuselage around the rudder shaft. (b) Maximum values of heat flux on the wall of the rudder shaft.

the gap. High speed flow cannot hit the shaft surface, and the maximum values of heat flux on the surface of the fuselage and rudder shaft do not increase.

IV. CONCLUSIONS

Numerical simulation of the restricted flow in the mounting gap of a controlled rudder is conducted by solving three-dimensional (3D) Reynolds-averaged Navier–Stokes equations. The primary emphasis of this paper is to identify the types of 3D separations, their patterns, and their mechanisms in producing extreme thermal environment in the mounting gap. We have seen how the characteristics, locations, and connections of singularities vary with the gap height ratio h/δ, which further indicates the significant change in types of flow separation occurring in the mounting gap. Once the topological and connection of these singularities are obtained, the general flow pattern in the gap is effectively determined, which enables us to pick out the flow physics of this complex three-dimensional flows. The conclusions can be drawn as follows:

(1) The vortex system in the mounting gap mainly exists in two modes. The first is the coexistence of tornado-type vortices and horseshoe-type vortices, and the second contains only horseshoe vortices. At a medium gap height

(h/δ = 0.28–0.64), the incoming flow experiences two types of global 3D separations and forms horseshoe vortices and tornado-type vortices around the rudder shaft. Then, the tornado-type vortex disappears with the increase of gap height ratio (h/δ > 0.85), and only left horseshoe vortices occur in the gap.

(2) The horseshoe vortex is the main cause of extreme localized heat flux on the fuselage and rudder shaft, while the tornado-type vortex prevents the production of high heat flux. The horseshoe vortex produces higher local heat flux by transporting fluid of high velocity and temperature toward the surface. The tornado-type vortex prevents the occurrence of this process by forming a zone of low-temperature backflow directly in front of the rudder shaft.

(3) The heat flux increases with the increase of gap height, as a result of the decrease of the region of low-speed backflow ahead of the rudder shaft. The positions of regions of localized high heat flux gradually move from the side to the center of the rudder shaft. The harshest thermal environment is created when the flow at high velocity enters the gap and arrives at the rudder shaft without separation halfway.

ACKNOWLEDGMENTS

AUTHOR DECLARATIONS

Conflict of Interest

The authors have no conflicts to disclose.

DATA AVAILABILITY

The data that support the findings of this study are available from the corresponding author upon reasonable request.

REFERENCES

[1] J. Fang, Y. Yao, A. A. Zheltovodov, and L. Lu, "Investigation of three-dimensional shock wave/turbulent-boundary-layer interaction initiated by a single fin," AIAA J. **55**, 509 (2016).

[2] Y. Lee, G. S. Settles, and C. C. Horstman, "Heat transfer measurements and computations of swept-shock-wave/boundary-layer interactions," AIAA J. **32**, 726 (1994).

[3] J. D. Pickles, B. R. Mettu, P. K. Subbareddy, and V. Narayanaswamy, "On the mean structure of sharp-fin-induced shock wave/turbulent boundary layer interactions over a cylindrical surface," J. Fluid Mech. **865**, 212 (2019).

[4] G. S. Settles and F. K. Lu, "Conical similarity of shock/boundary-layer interactions generated by swept and unswept fins," AIAA J. **23**, 1021 (1985).

[5] L. Brusniak and D. S. Dolling, "Physics of unsteady blunt-fin-induced shock wave/turbulent boundary layer interactions," J. Fluid Mech. **273**, 375 (2006).

[6] D. S. Dolling, "Comparison of sharp and blunt fin-induced shock wave/turbulent boundary-layer interaction," AIAA J. **20**, 1385 (1982).

[7] C.-M. Hung and P. Buning, "Simulation of blunt-fin-induced shock-wave and turbulent boundary-layer interaction," J. Fluid Mech. **154**, 163 (1985).

[8]X. Zhao, H. Hu, and L. Zhao, "Effect of an adverse pressure gradient on hypersonic wall pressure fluctuations," Phys. Fluids **33**, 106107 (2021).

[9]M. Mortazavi and D. Knight, "Simulation of hypersonic-shock-wave–laminar-boundary-layer interaction over blunt fin," AIAA J. **57**, 3506 (2019).

[10]T. J. Horvath, S. A. Berry, N. R. Merski, and S. M. Fitzgerald, "X-38 experimental aerothermodynamics," J. Spacecr. Rockets **41**, 272 (2004).

[11]W. Deveikis and W. Bartlett, "Pressure and heat-transfer distributions in a simulated wing-elevon cove with variable leakage at a free-stream Mach number of 6.9," in *Technical Report NASA TM-74095* (American Institute of Aeronautics and Astronautics, 1978).

[12]R. Hunt, "Aerothermal environment in chordwise gaps between split elevons at Mach 6.8," Report No. NASA-TP-1783, 1980.

[13]A. Wieting, J. Walsh, and K. Bey, "Aerothermal environment in control surface gaps in hypersonic flow—An overview," AIAA Paper No. 1983-1483, 1983.

[14]H. Wong and F. G. J. Kremer, "Numerical assessment on the heating of the rudder/fin gap in X-38 space vehicle," in *International Symposium On Atmospheric Reentry Vehicles and Systems, French Association for Aeronautics and Astronautics* (Arachon, France, 1999), pp. 1–10.

[15]J. Dunlap, B. Steinetz, D. Curry, J. DeMange, and H. Rivers, "Investigations of control surface seals for re-entry vehicles," AIAA Paper 2002-3941, 2002.

[16]R. Alviani, G. A. Blaisdell, and J. Poggie, "Computational analysis of planned high-speed swept wing-elevon experiments," AIAA Paper 2022-2198, 2022.

[17]R. Alviani, J. Poggie, and G. Blaisdell, "Detached eddy simulation of supersonic wing-elevon cove boundary-layer ingestion," AIAA Paper 2020-3008, 2020.

[18]R. Alviani, J. Poggie, and G. Blaisdell, "Unsteady aspects of shock-wave/boundary-layer interaction resulting from control surface deflection," AIAA Paper 2021-2823, 2021.

[19]J. M. Lei, Y. Zhang, and Z. W. Zheng, "Numerical simulation of heating over the rudder shaft gap in hypersonic flow," Procedia Eng. **67**, 412 (2013).

[20]A. Winkelmann, "Experimental investigations of a fin protuberance partially immersed in a turbulent boundary layer at Mach 5," Silver Spring: Naval Ordnance Lab Report No.:NOLTR, 72-33 (1972).

[21]R. Neumann and J. Hayes, "Aerodynamic heating in the fin interaction region of generalized missile shapes at Mach 6 (modular missile test program)," Report No. TR 79-3066, Air Force Flight Dynamic Laboratory, Wright-Patterson AFB, OH, 1979.

[22]R. Alviani, D. Fano, J. Poggie, and G. Blaisdell, "Aerodynamic heating in the gap between a missile body and a control fin," J. Spacecr. Rockets (published online) (2022).

[23]D. Fano, J. Poggie, and G. Blaisdell, "Aerodynamic heating in missile-fin interaction region," AIAA 2020-0583, 2020.

[24]Q. Li, L. Nie, K. Zhang, Y. Li, S. Chen, and G. Zhu, "Experimental investigation on aero-heating of rudder shaft within laminar/turbulent hypersonic boundary layers," Chin. J. Aeronaut. **32**, 1215 (2019).

[25]F. Zhang, S. Yi, X. Xu, H. Niu, and X. Lu, "A swept fin-induced flow field with different height mounting gaps," Chin. J. Aeronaut. **34**, 148 (2021).

[26]S. A. Gbadebo, N. A. Cumpsty, and T. P. Hynes, "Three-dimensional separations in axial compressors," J. Turbomachinery **127**, 331 (2005).

[27]J. Anderson, *Fundamentals of Aerodynamics* (McGraw Hill Higher Education, 2005).

[28]U. Goldberg, O. Peroomian, and S. Chakravarthy, "A wall-distance-free k-ε model with enhanced near-wall treatment," J. Fluids Eng. **120**, 457 (1998).

[29]J. Peng, C. T. Luo, Z. J. Han, Z. M. Hu, G. L. Han, and Z. L. Jiang, "Parameter-correlation study on shock–shock interaction using a machine learning method," Aerosp. Sci. Technol. **107**, 106247 (2020).

[30]Z. Zhang, C. Wen, W. Zhang, Y. Liu, and Z. Jiang, "Formation of stabilized oblique detonation waves in a combustor," Combust. Flame **223**, 423 (2021).

[31]H. Lu, L. Yue, Y. Xiao, and X. Zhang, "Interaction of isentropic compression waves with a bow shock," AIAA J. **51**, 2474 (2013).

[32]E. Schülein and A. Zheltovodov, "Documentation of experimental data for hypersonic 3-D shock waves," DLR, German Aerospace Center Internal Report IB 223-99 A 26, 95 (2001).

[33]T. J. Leger and J. Poggie, "Computational analysis of shock wave turbulent boundary layer interaction," in *52nd Aerospace Science Meeting* (American Institute of Aeronautics and Astronautics, 2014) AIAA Paper No. 2014-0951.

[34]T. R. Bewley and B. Protas, "Skin friction and pressure: The 'footprints' of turbulence," Physica D **196**, 28 (2004).

[35]T. Liu, "Skin-friction and surface-pressure structures in near-wall flows," AIAA J. **56**, 3887 (2018).

[36]T. Liu, "Global skin friction measurements and interpretation," Prog. Aerosp. Sci. **111**, 100584 (2019).

[37]H. Poincaré, *Oeuvres de Henri Poincaré: Tome 1* (Gauthier-Villars, Paris, 1928).

[38]R. Legendre, "Séparation de l'ecoulement laminaire tridimensionnel," La Recherche Aérospatiale **54**, 3–8 (1958).

[39]M. J. Lighthill, "Attachment and separation in three-dimensional flow," in *Laminar Boundary Layers Theory*, Vol. II, 2.6 (Oxford University Press, Oxford, 1963), pp. 72–82.

[40]A. E. Perry and M. S. Chong, "A description of eddying motions and flow patterns using critical-point concepts," Annu. Rev. Fluid Mech. **19**, 125 (1987).

[41]G. T. Chapman and L. A. Yates, "Topology of flow separation on three-dimensional bodies," Appl. Mech. Rev. **44**, 329 (1991).

[42]L. A. Yates and G. T. Chapman, "Streamlines, vorticity lines, and vortices around three-dimensional bodies," AIAA J. **30**, 1819 (1992).

[43]D. Simmons, F. O. Thomas, and T. C. Corke, "Smooth body flow separation experiments and their surface flow topology characterization," in *AIAA Aviation 2019 Forum* (American Institute of Aeronautics and Astronautics, 2019).

[44]R. R. Pulimidi and F. K. Lu, "On the three-dimensional separation in shock/boundary-layer interactions at swept corners," in *AIAA Aviation 2019 Forum* (American Institute of Aeronautics and Astronautics, 2019).

[45]S. Chen, W. Zhao, and D. Wan, "Turbulent structures and characteristics of flows past a vertical surface-piercing finite circular cylinder," Phys. Fluids **34**, 015115 (2022).

[46]J. M. Délery, "Physics of vortical flows," J. Aircr. **29**, 856 (1992).

[47]J. M. Délery, "Robert Legendre and Henri Werlé: Toward the elucidation of three-dimensional separation," Annu. Rev. Fluid Mech. **33**, 129 (2001).

[48]H. G. Hornung and A. E. Perry, "Some aspects of three-dimensional separation. Part I: Streamsurface bifurcations," Z. Flugwiss. Weltraumforsch. 8, 77–87 (1984).

[49]T. Hsieh and K. C. Wang, "Three-dimensional separated flow structure over a cylinder with a hemispherical cap," J. Fluid Mech. **324**, 83 (1996).

[50]A. Surana, G. B. Jacobs, and G. Haller, "Extraction of separation and attachment surfaces from three-dimensional steady shear flows," AIAA J. **45**, 1290 (2007).

[51]B. Lazos, "Surface topology on the wheels of a generic four-wheel landing gear," AIAA J. **40**, 2402 (2002).

[52]J. C. R. Hunt, C. J. Abell, J. A. Peterka, and H. Woo, "Kinematical studies of the flows around free or surface-mounted obstacles; applying topology to flow visualization," J. Fluid Mech. **86**, 179 (1978).

[53]D. Sun, Q. Guo, C. Li, and P. Liu, "Direct numerical simulation of effects of a micro-ramp on a hypersonic shock wave/boundary layer interaction," Phys. Fluids **31**, 126101 (2019).

[54]G. Nasif, R. Balachandar, and R. M. Barron, "Influence of bed proximity on the three-dimensional characteristics of the wake of a sharp-edged bluff body," Phys. Fluids **31**, 025116 (2019).

[55]H.-X. Huang, H.-J. Tan, S. Sun, and Y. Ling, "Evolution of supersonic corner vortex in a hypersonic inlet/isolator model," Phys. Fluids **28**, 126101 (2016).

[56]M. Tobak and D. J. Peake, "Topology of three-dimensional separated flows," Annu. Rev. Fluid Mech. **14**, 61 (1982).

[57]A. Surana, O. Grunberg, and G. Haller, "Exact theory of three-dimensional flow separation. Part 1. Steady separation," J. Fluid Mech. **564**, 57 (2006).

[58]S. Hosseinverdi, R. Jacobi, and H. F. Fasel, "Topology and flow structures of three-dimensional separation bubbles: The effect of aspect ratio," AIAA 2015-2630, 2015.

[59]M. J. Khan and A. Ahmed, "Topological model of flow regimes in the plane of symmetry of a surface-mounted obstacle," Phys. Fluids **17**, 045101 (2005).

[60]M. F. Blair, "Heat transfer in the vicinity of a large-scale obstruction in a turbulent boundary layer," J. Propul. Power **1**, 158 (1985).

[61]G. Taylor and I. Gursul, "Unsteady vortex flows and buffeting of a low sweep delta wing," in *AIAA Paper 2004-1066* (American Institute of Aeronautics and Astronautics, 2004).